

www.acsami.org Research Article

# Electrogenerated Chemiluminescence and Spectroelectrochemistry Characteristics of Blue Photoluminescence Perovskite Quantum Dots

Jeetika Yadav, Qiaoli Liang, and Shanlin Pan\*



Cite This: ACS Appl. Mater. Interfaces 2020, 12, 27443-27452



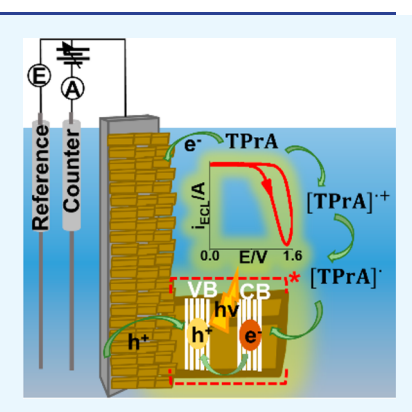
**ACCESS** 

III Metrics & More



Supporting Information

ABSTRACT: Lead-based perovskite MAPbX<sub>3</sub> (MA = CH<sub>3</sub>NH<sub>3</sub>, X = Cl and Br) has shown great potential benefits to advance modern optoelectronics and clean energy harvesting devices. Poor structural stability is one of the major challenges of MAPbX<sub>3</sub> perovskite materials to overcome to achieve desired device performance. Here, we present the electrochemical stability study of CH<sub>3</sub>NH<sub>3</sub>PbCl<sub>1.08</sub>Br<sub>1.92</sub> quantum dots (QDs) by electrogenerated chemiluminescence (ECL) and photoluminescence (PL) spectroelectrochemistry methods. Electrochemical anodization of pristine MAPbX<sub>3</sub> QD film results in the disproportionate loss of methylammonium and halide ions (X = Cl and Br). ECL efficiency and stability of perovskite QDs in the presence of coreactant tripropyl amine (TPrA) can be greatly improved after being incorporated into a polystyrene (PS) matrix. Mass spectrum and X-ray photoelectron spectroscopy (XPS) measurements were used to provide chemical composition variation details of QDs, which are responsible for the ECL and PL characteristics (e.g., wavelength redshift) of perovskite QDs in an electrochemical cell.



KEYWORDS: perovskite, quantum dots (QDs), nanocrystals, polystyrene (PS), electrogenerated chemiluminescence (ECL), photoluminescence (PL), Blue light emission

rganometallic halide perovskites such as MAPbX<sub>3</sub> (MA =  $CH_3NH_3$ , X = Cl and Br) have emerged as a new candidate for solar cells, 1-4 lasers, 5-7 and light-emitting diodes (LEDs).8-11 Their emission and absorption can be tuned in a broad wavelength range by simply changing their nanocrystal sizes and types of halide ions, 12-21 and shapes from 2D perovskite nanosheets to 0D perovskite quantum dots.<sup>22</sup> Nanostructured organometallic halide perovskites have unique emission characteristics such as high absorption coefficient,<sup>2</sup> narrow full width at half maxima (fwhm), 23 color purity, 24 and high photoluminescence (PL) quantum yield and photo-stability, <sup>23,25,26</sup> For example, Zhang et al.<sup>25</sup> synthesized colortunable and narrow band emissive CH3NH3PbBr3 colloidal quantum dots (QDs) using a ligand-assisted reprecipitation (LARP) technique. Huang et al.<sup>27</sup> developed a temperature reprecipitation method for CH3NH3PbBr3 QDs with tunable PL in the range of 475 to 570 nm. MAPbX<sub>3</sub> perovskite QDs have nearly unity PL quantum yield, narrow emission line width, and low defect density;<sup>28,29</sup> therefore, they are among ideal candidates for efficient LEDs and electrogenerated chemiluminescence (ECL). ECL is a light generation process from an excited-state species formed by electron transfer reaction between electrochemically produced oxidized and reduced state species.<sup>30</sup> Recent studies suggest ECL can be produced from perovskite QDs. CH3NH3PbBr3 QDs exhibit ECL emission in aqueous media in either coreactant or annihilation ECL pathways. 23,31 CsMBr<sub>3</sub> (M = Pb and Bi)

QDs with various shapes and sizes have been synthesized for studying their ECL activities in either annihilation or coreactant route. <sup>24,26,28,29,32-35</sup> Cao et al. synthesized environmentally friendly CsBiBr<sub>3</sub> perovskite QDs using the LARP technique and obtained stable and efficient ECL response. Poor structural stability is one of the major challenges of organometallic halide perovskite QDs that need to be overcome to achieve desired optical and electrochemical properties. Halide ion migration, defects, and structure decomposition when exposed to air, heat, moisture, and UV irradiation are among the causes of the stability issues of organometallic halide perovskites. New synthesis methodology and structural engineering techniques are needed to obtain stable perovskite crystal structure for optimal light absorption and carrier transport and stability. 36-39 Our team recently demonstrated blue ECL and single QD PL imaging of mixed halide perovskite QDs of CH3NH3PbCl1.08Br1.92 on glassy carbon electrode. 40 Two distinct ECL peaks at 473 and 745 nm were obtained when ECL was produced with coreactant of

Received: January 17, 2020 Accepted: May 14, 2020 Published: May 14, 2020





tripropyl amine (TPrA). The major challenges of this study are the poor stability of QD film and mystery of the new redshifted ECL peak above 600 nm. Here, we present ECL and PL spectroelectrochemistry characteristics of MAPbX<sub>3</sub> (X= Cl and Br) QDs incorporated into polystyrene (PS) matrix with enhanced efficiency and stability.

## ■ RESULTS AND DISCUSSION

Structural and Morphological Characteristics of QDs-Tol and QDs-PS. The composition of as-synthesized perovskite QDs is CH<sub>3</sub>NH<sub>3</sub>PbCl<sub>1.08</sub>Br<sub>1.92</sub> and is referred to as QDs throughout the manuscript. As shown in Figure 1a, b,

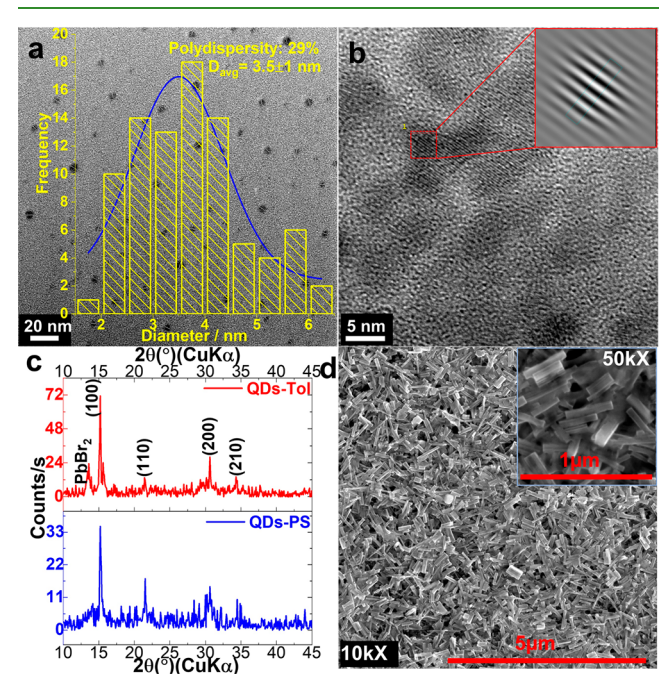


**Figure 1.** (a) Transmission electron micrograph (TEM) image of  $CH_3NH_3PbCl_{1.08}Br_{1.92}$  QDs along with a histogram of the QDs diameters showing an average diameter of 3.5  $\pm$  1.0 nm. (b) High-resolution TEM image of QDs. (c) XRD pattern of QDs-Tol/ITO and QDs-PS/ITO and (d) SEM image of QDs-Tol film drop-casted on ITO.

as-synthesized perovskite QDs show an average diameter of 3.5 ± 1.0 nm and a lattice spacing of 0.307 nm. The polydisperse size distribution is expected because of the room-temperature synthesis approach using the ligand-assisted reprecipitation method as described in detail in the experimental section. The QDs-Tol and QDs-PS films were structurally characterized by X-ray diffraction (XRD). Figure 1c shows the XRD pattern for QDs-Tol (red) and QDs-PS (blue) coated onto an indium tin oxide (ITO) electrode. Two major diffraction peaks are observed at  $2\theta = 15.1$  and  $30.6^{\circ}$  along with minor peaks at 21.6 and 34.2°, corresponding to the reflections from 100, 200, 110, and 210 cubic phase structure, respectively. 27,41 The sharp peaks denote the formation of bulk large crystallites. The crystallite size for the QDs-Tol and QDs-PS was calculated using the Debye-Scherrer's equation 41 to be 44.3 and 19.0 nm, respectively. The increase in crystallite sizes in Figure 1d as compared to the initial-synthesized QDs shown in Figure 1a, b is caused by the QD self-assembly to form large crystals after being coated onto an electrode surface. As shown in Figure 1d, nanorods (NRs) of perovskite are formed upon the

aggregation of QDs. The NR morphology depends on the self-assembly of QDs in the presence of n-octyl amine and oleic acid and solvent evaporation conditions. Details of the anisotropic NR formation mechanism need further investigation.

Absorption and PL Spectra of Perovskite QD Solutions and Films. The QDs in toluene (QDs-Tol) and QDs dispersed in 0.09 wt % polystyrene (QDs-PS) were drop-casted onto ITO and then vacuum-dried for the subsequent ECL investigation. As shown in Figure 2a, the UV-vis

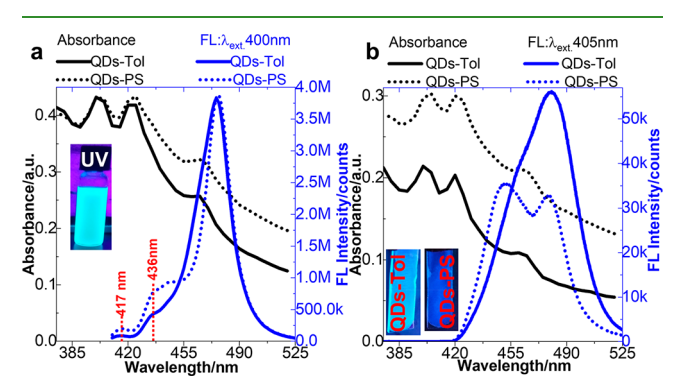


**Figure 2.** (a) Absorption and PL spectra of CH<sub>3</sub>NH<sub>3</sub>PbCl<sub>1.08</sub>Br<sub>1.92</sub> QDs solution in the absence (QDs-Tol) and presence of polystyrene (QDs-PS). (b) Absorption and PL spectra QDs thin film coated from QDs-Tol and QDs-PS solutions onto ITO glass. The insets are photos of QDs-Tol solution and QDs-PS films under UV lamp excitation.

absorption spectra of the QDs-Tol and QDs-PS solution samples have a band edge of 464.9 nm. Both QDs-Tol and QDs-PS solutions show a PL emission peak at 475 nm in addition to two weak peaks located at 417 and 436 nm. QDs-Tol and QDs-PS solutions have relatively small Stokes shift of 10.1 and 11.1 nm, respectively, originating from direct exciton recombination. The insets in Figure 2a show a PL photo of a QDs-Tol solution under UV lamp excitation. Figure 2b shows the UV-vis absorption spectra of the QDs-Tol and QDs-PS films on ITO with a band edge of 460 nm. The QDs-Tol film has two PL peaks at 451.8 and 480.8 nm with fwhm's of 28.6 and 37.2 nm, respectively, as shown in Figure S1. The PL spectrum of QDs-PS film on ITO shown in Figure 2b shows two separated emission peaks (Figure S1) at 449 and 478.4 nm with fwhm's of 26.7 and 30.1 nm, respectively. Both the samples demonstrate bright blue emission under 405 nm laser excitation. The inset in Figure 2b shows the PL photos of QDs-Tol and QDs-PS films under UV excitation. The lifetime of the QDs dispersed in toluene is 1.0 ns as shown in Figure

Redox Properties and ECL Characteristics of Perovskite QD Films. ECL was performed for the QDs-Tol film in 0.1 M TBAPF<sub>6</sub> in acetonitrile with 50 mM TPrA. The cyclic voltammograms (CV) and the corresponding ECL of the QDs on ITO film are shown in Figure 3. The bare ITO electrode does not produce any oxidation peaks and ECL emission in the absence of TPrA. No ECL was obtained from any QD-modified ITO electrode in the absence of TPrA, although there is an irreversible oxidation peak of QDs on ITO above 1.20 V (vs SCE). ECL was not produced with bare ITO in the presence of TPrA, although direct oxidation of TPrA can be obtained above 0.90 V (vs SCE). In the presence of TPrA, the anodic current of 4.5 mA and ECL response of 2.2  $\mu$ A are obtained from the QD-modified ITO electrode. The

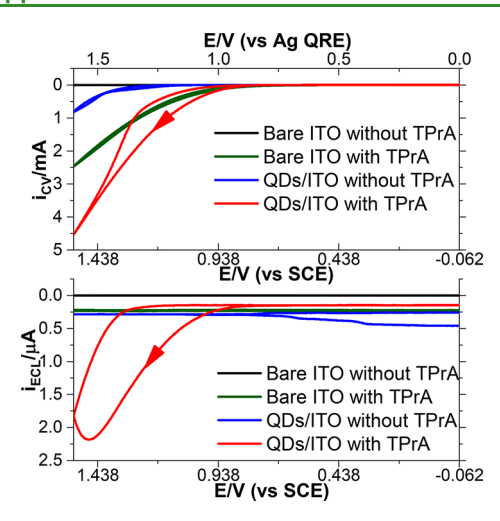


**Figure 3.** CVs (top) and ECL (bottom) responses from CH<sub>3</sub>NH<sub>3</sub>PbCl<sub>1.08</sub>Br<sub>1.92</sub> QD-modified (QD-Tol) ITO in 0.1 M TBAPF<sub>6</sub> in acetonitrile with and without 50 mM TPrA.

mechanism of the ECL generation from QDs is shown in eqs 1-5:

$$QDs - e^{-} \rightarrow QDs^{+}$$
 (1)

$$TPrA - e^{-} \rightarrow TPrA^{+} \tag{2}$$

$$TPrA^{+} - H^{+} \rightarrow TPrA \tag{3}$$

$$QDs^{+} + TPrA \rightarrow QDs^{*} + products$$
 (4)

$$QDs^* \rightarrow QDs + h\nu$$
 (5)

TPrA is anodized to TPrA<sup>+•</sup> and QDs are oxidized to form QDs<sup>+•</sup> upon positive potential scan in the presence of TPrA. The TPrA<sup>+•</sup> then releases a proton to generate a strong reducing radical intermediate, TPrA<sup>•</sup>. QDs<sup>+•</sup> undergo an electron transfer reaction with TPrA<sup>•</sup> to generate QDs in excited-state QDs\*, leading to an intense ECL emission.

CH<sub>3</sub>NH<sub>3</sub>PbCl<sub>1.08</sub>Br<sub>1.92</sub> QDs in this study are synthesized in the presence of oleic acid and n-octyl amine, which are necessary to passivate the surface defect sites.<sup>32</sup> However, the conductivity of these ligands is poor and it will prevent charge transport when QDs are transferred into a solid film for ECL study. To understand how the presence of oleic acid and noctyl amine affects the redox activities and ECL performance of CH<sub>3</sub>NH<sub>3</sub>PbCl<sub>1.08</sub>Br<sub>1.92</sub> QDs, we washed as-synthesized QDs with toluene as the ligand density control. We performed CVs as a function of toluene washing as shown in Figure S3. Our results show less anodic current and ECL are obtained for as-

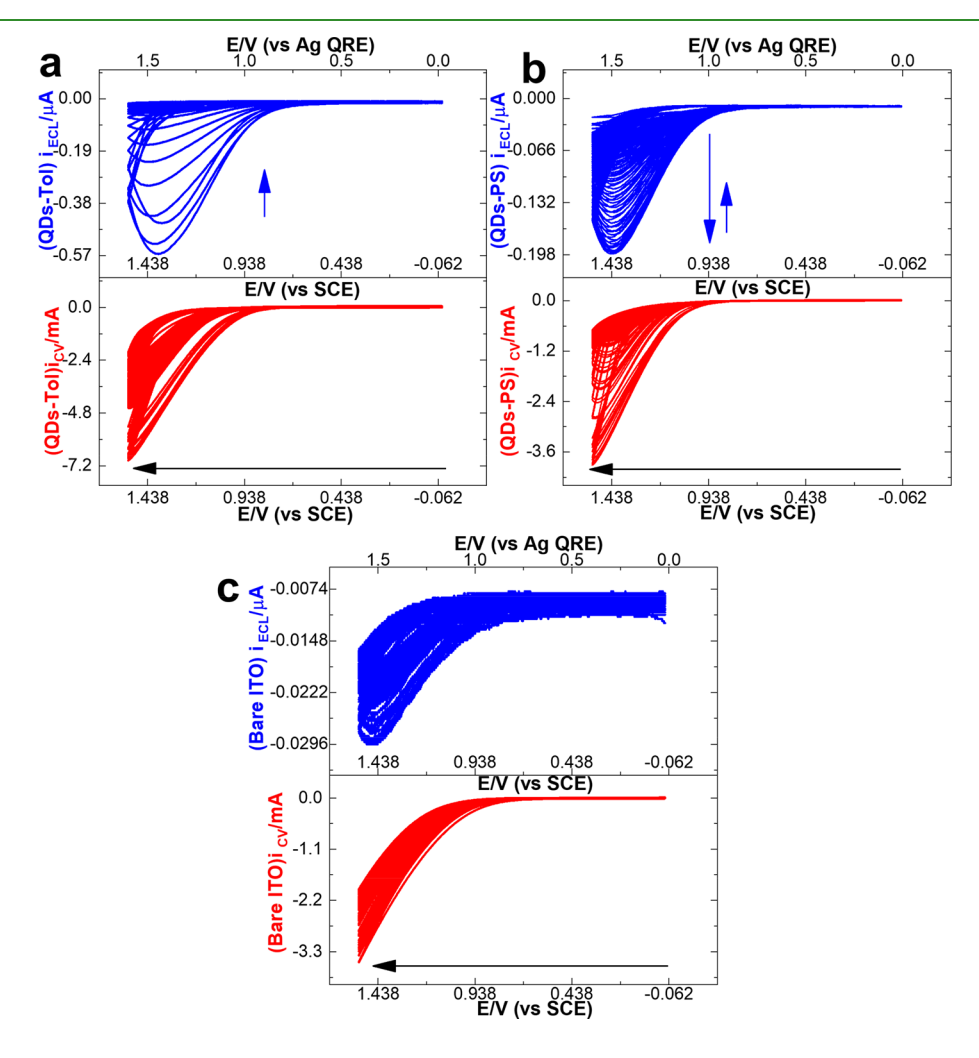


Figure 4. Top (blue) and bottom (red) panels show the overlay of ECL current (denoted by blue) and CV current (denoted by red), respectively, for 100 cycles for (a) CH<sub>3</sub>NH<sub>3</sub>PbCl<sub>1.08</sub>Br<sub>1.92</sub> QDs-Tol film on ITO, (b) QDs-PS film on ITO, and (c) bare ITO in 0.1 M TBAPF<sub>6</sub> with 50 mM TPrA in acetonitrile.

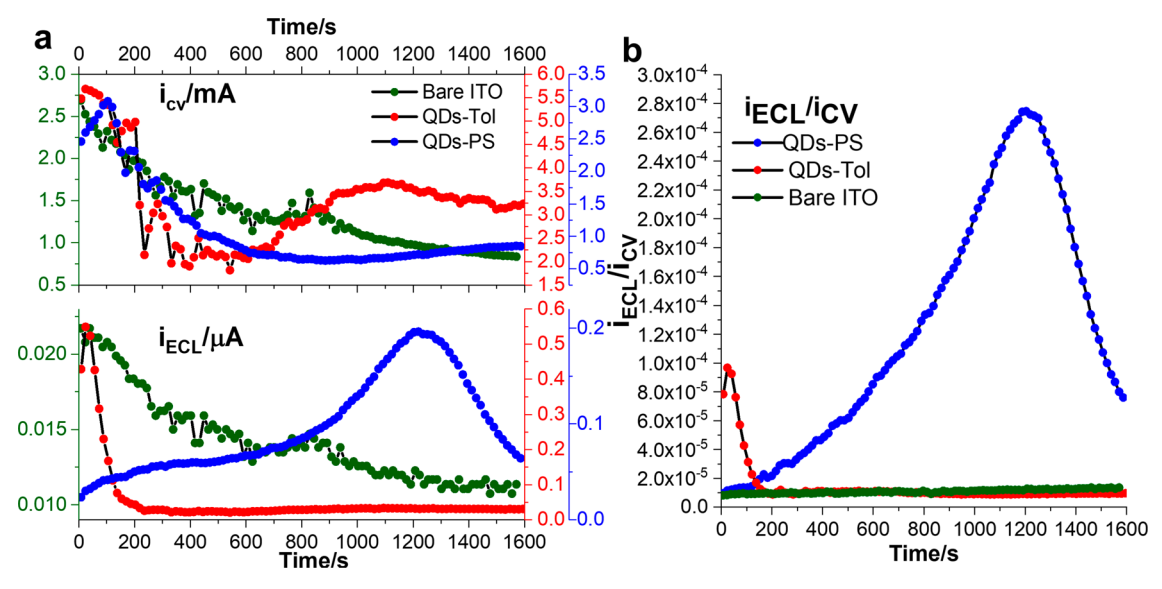
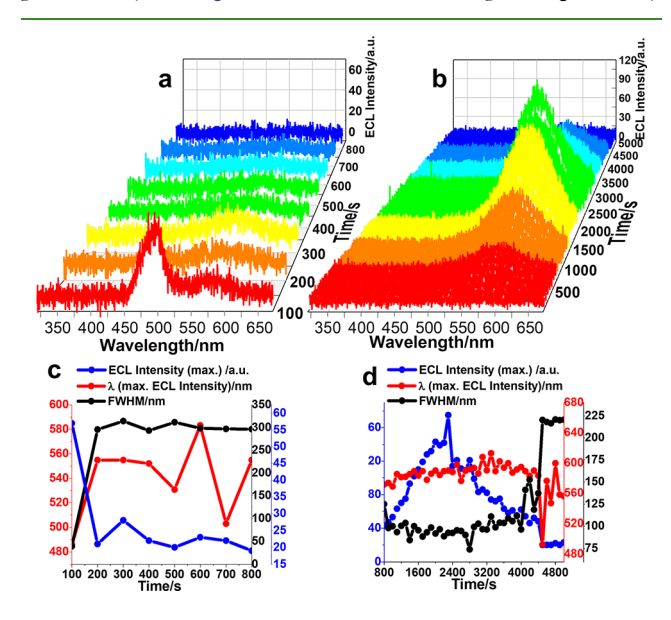


Figure 5. (a) Anodic current (top panel) and the corresponding ECL (bottom panel) trajectories of  $CH_3NH_3PbCl_{1.08}Br_{1.92}$  QDs-Tol (red), QDs-PS (blue), and bare ITO (green) at 1.44 V (vs SCE) and (b) the ratio of ECL current to CV current ( $i_{ECL}/i_{CV}$ ) for evaluating ECL efficiency. All data are extracted from CVs of Figure 4.

synthesized QD than toluene-washed samples. This is because the presence of excessive ligands without the toluene washing prevents the efficient charge injection and transport. However, poor film stability and sample aggregation are the major problems of QDs treated with excessive toluene purification. Therefore, QDs washed with toluene once are used in all the following measurements.

ECL Stability and Intensity of Perovskite QD Films and Effect of PS Matrix. ECL stability of CH<sub>3</sub>NH<sub>3</sub>PbCl<sub>1.08</sub>Br<sub>1.92</sub> QDs drop-casted on ITO directly from QDs-Tol was evaluated for 100 CV cycles as shown in Figure 4a. The ECL response decreases gradually because of the poor structural stability upon electrochemical anodization. To stabilize the QD ECL and stability of the QD film on ITO, we drop-casted QD films directly from QDs-PS containing polystyrene to help improve the stability of QDs on ITO for ECL study. Figure 4b shows the CV and the corresponding ECL response from the QD film from QDs-PS. Surprisingly, the ECL response initially increases, reaches a maximum, and then decreases gradually. Figure 4c shows a control experiment with only a bare ITO in the presence of TPrA for 100 CV cycles. Only a very weak ECL signal can be obtained. It is not clear where the background ECL of bare ITO comes from. It is likely from the impurities of TPrA and solvent. Figure 5a shows the current and the corresponding ECL intensity for the film samples of QDs-Tol, QDs-PS, in comparison with the bare ITO at 1.44 V (vs SCE). All these current and ECL data are extracted directly from ECL and CVs in Figure 4. Anodic current at the bare ITO decreases gradually while producing a weak ECL signal. The anodic current feature of QDs-Tol includes a gradual decay throughout the first 600 s and then an increase, producing only a short-lived ECL. The anodic current of QDs-PS, however, increases for the first 100 s, followed by a continuous decrease. The ECL response of QDs-Tol and the bare ITO decreases upon CV cycling, whereas the QDs-PS ECL response increases throughout the first 1200 s and then decreases. To better illustrate the ECL/current features of all three samples, we plotted the ratio of ECL intensity and anodization current,  $i_{ECL}/i_{CV}$ , to estimate the general trend of ECL efficiency<sup>31</sup> during the CV cycling, as shown in Figure 5b. The  $i_{\rm ECL}/i_{\rm CV}$  of the QDs-PS film increases for the first 1200 s and then decreases gradually. The  $i_{\rm ECL}/i_{\rm CV}$  of the QDs-Tol film increases briefly for the first 25 s and then decreases thereafter. A 2.6-fold increase in  $i_{\rm ECL}/i_{\rm CV}$  is observed for the QDs-PS film as compared to the QDs-Tol film. Bare ITO only has stable and weak  $i_{\rm ECL}/i_{\rm CV}$  response because of the weak ECL intensity in contrast to OD-modified films.

Figure 6 shows the stability characteristics of the ECL spectrum. The ECL spectrum of the QDs-Tol film shows an unstable peak at 492.0 nm that disappears after the first potential cycle. Figure 6c shows the corresponding stability



**Figure 6.** Time evolution of ECL spectrum of (a) CH<sub>3</sub>NH<sub>3</sub>PbCl<sub>1.08</sub>Br<sub>1.92</sub> QDs-Tol and (b) QDs-PS during potential stepping between 1.54 V and -0.06 V (vs SCE) for 100 steps with 1 s pulse width for 8 and 50 consecutive cycles, respectively. (c, d) Time evolutions of fwhm maximum ECL intensity and wavelength at maximum ECL intensity of the QDs-Tol and QDs-PS films, respectively.

trajectories in fwhm (full width at half maxima), maximum ECL intensity, and the wavelength at maximum ECL intensity. Both ECL intensity and fwhm decrease upon anodization of the QD film. The initial ECL peak at 492.0 nm is accompanied by another longer wavelength peak at 578.0 nm, which is more stable than the 492.0 nm peak for extended anodization cycling. Figure 6b shows the ECL spectra of the QDs-PS film, with a single peak at 590.4 nm increasing slowly with each potential stepping. This ECL peak reaches a maximum at 2300 s and then decreases thereafter. Figure 6d shows the corresponding evolutions of ECL intensity, the wavelength at maximum ECL intensity, and the fwhm. The wavelength at maximum ECL intensity remains constant for the most part for QDs-PS film. The ECL intensity reaches a maximum accompanied by a gradual decrease in its fwhm, and then ECL intensity decreases, accompanied by a gradual increase in its fwhm. The ECL from the QDs-Tol film shows poor stability only because of the dissolution of solid QDs into the electrolyte solution and structural loss upon anodization. On the other hand, the ECL from the QDs-PS film is stable enough for 20-40 min under the potential cycling conditions. It indicates that polystyrene helps improve the ECL stability of CH<sub>3</sub>NH<sub>3</sub>PbCl<sub>1.08</sub>Br<sub>1.92</sub> QDs by acting as a scaffold to prevent leakage of QDs and X ions into electrolyte solution while still allowing oxidation of TPrA for ECL generation.

The difference in the initial ECL wavelength and stability of QDs-Tol ECL and QDs-PS films has to do with the electrochemical stability and particle aggregation characteristics when loaded onto ITO. The initial short ECL wavelength at 492.0 nm of QDs-Tol film is assigned to small QD aggregates or QDs loosely bonded to the ITO surface, which lose their activities quickly during the initial potential cycling. The longer ECL peak at 578.0 nm in Figure 6a is likely associated with larger aggregates when QDs are close to each other. Disproportionate loss halide ions, as shown in our XPS data, may contribute to the new ECL peak. The ECL of the QDs-PS film is from QD aggregates stabilized by high refraction index polymer matrix. We hypothesize that only the QDs near the polymer surface and close to electrolyte solution are ECL active. QDs buried inside the polymer film are ECL inactive. Solvent-assisted swelling of polystyrene may also allow TPrA molecules to transport through QD film, so they can be oxidized to produce red-shifted ECL at 590.4 nm (Figure 6b). The ECL mechanism of QD-PS sample is describe by eqs 6-10.

$$TPrA - e^{-} \rightarrow TPrA^{+}$$
 (6)

$$TPrA^{+} - H^{+} \rightarrow TPrA \tag{7}$$

$$QDs + TPrA \rightarrow QDs^{-}$$
 (8)

$$TPrA^{+} + QDs^{-} \rightarrow QDs^{*}$$
 (9)

$$QDs^* \rightarrow QDs + hv$$
 (10)

Figure S4a shows the overlay of PL spectra with the ECL spectra for the QDs-Tol film. The two distinct PL peaks of QDs-Tol film are located at 451.8 and 480.8 nm, respectively. ECL peaks are located at 492.2 nm (fwhm of 38.4 nm) and 578.7 nm (fwhm of 88.6 nm), respectively. The redshift of ECL is due to the presence of electrolyte and solvent, and only those QDs activated by electrochemical reaction emit light, in contrast to photoexcitation processes, which can excite all QDs inside the film sample.<sup>32</sup> Besides, ECL is a surface-sensitive

light process.<sup>42</sup> It is affected by the surface states and the surface ligands on QDs. Red-shifted ECL has been previously observed when the excited-state electrons relax into surface states of QDs.<sup>43</sup> Figure S4b shows the ECL and PL spectra of QDs-PS film. The PL peaks are observed at 449 and 478.4 nm, whereas the ECL peak is observed at 590.4 nm (fwhm of 92.5 nm).

PL Spectra of Fresh and ECL of Anodized Perovskite QD Films. Figure 7a shows the PL spectra of the QDs-Tol film

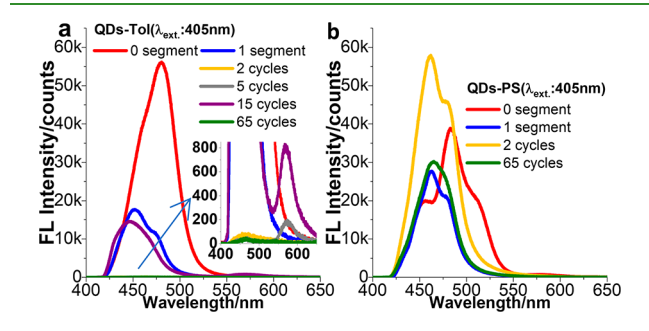


**Figure 7.** PL spectra of fresh-made film versus ECL anodized film for (a) QDs-Tol collected after 0, 0.5, 2, 5, 15, and 65 CV cycles and for the (b) QDs-PS films after 0, 0.5, 2, and 65 CV cycles. CV scan rate 0.2 V/s with potential scanned from 0 to 1.6 V vs SCE and Pt wire as counter electrode in 0.1 M TBAPF $_6$  in 50 mM TPrA in acetonitrile.

before and after CV cycling treatment. The corresponding normalized PL spectra for the QDs-Tol film are shown in Figure S5. The wavelength at maximum PL intensity is observed at 480.5 nm (fwhm = 47.3 nm), 451.5 nm (fwhm = 45.5 nm), 455.5 nm (fwhm = 118.2 nm), 572.7 nm (fwhm = 45.1 nm), 446.3 nm (fwhm = 46.2 nm), and 464.7 nm (fwhm = 282.9 nm) when processed with 0, 0.5, 2, 5, 15, and 65 CV cycles, respectively. The PL red-shifted with the maxima at 572.7 nm with a smaller blue-shifted peak at 465.5 nm after the first 5 consecutive cycles of potential scans. These PL peak positions are consistent with the ECL spectrum in Figure 6, although the relative light intensity and stability are determined by ECL reaction kinetics. Similarly, two peaks are observed for the PL after 15 consecutive cycles, with the major peak being at 446.3 nm with a smaller hump at 570.5 nm (Figure S5). Figure 7b shows the PL spectra of QDs-PS film before and after CV cycles. The overall PL stability of the QDs with PS can be seen from Figure 7a, b. The PL intensity of the QDs-Tol film is significantly reduced to 41 counts after 65 cycles, whereas the PL intensity of QDs-PS film remains at 30235.6 counts even after 65 cycles.

XPS Characterization of QDs-Tol Film before and after ECL. XPS was performed for the QDs-Tol film before and after electrochemical anodization, as shown by the corresponding low-resolution XPS spectra and quantification selected peaks are shown in Figures S6 and S7, respectively. Figure 8 shows selected high-resolution XPS spectra of C 1s, N 1s, O 1s, Cl 2p with P 2s, Br 3d ,and Pb 4f when processed with 0, 1, 15 CV cycles. Figure 8a depicts the evolution of XPS C 1s core-level spectra when processed with 0, 1, and 15 CV cycles. The C 1s core-level spectra for the 0 CV cycles shows two major contributions, one at 285.3 eV representing the C-N bond due to the methylammonium cation 44 and the other at 288.7 eV, which is attributed to C-O species O=C-O<sup>45</sup> or COCH<sub>3</sub>. C 1s core level spectrum shifts to higher binding energy denoting the dissociation of the C-N bond, which may

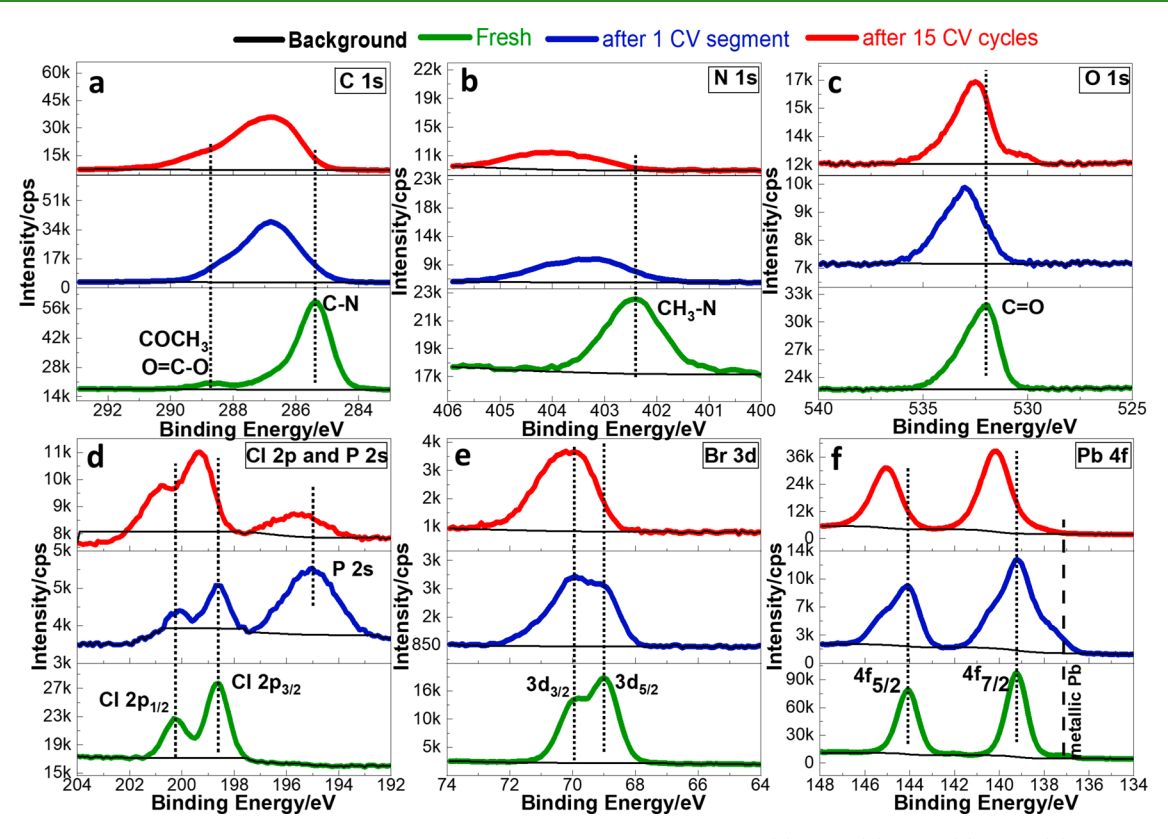


**Figure 8.** XPS characterization core level spectra of QDs-Tol film as a function of CV cycles (a) C 1s, (b) N 1s, (c) O 1s, (d) Cl 2p and P 2s, (e) Br 3d, and (f) Pb 4f core level spectra. The dashed lines are the guides for the eye. The black line represents the background. Green, blue and the red lines represent the QDs-Tol film fresh, after 1 CV segment and after 15 CV cycles, respectively.

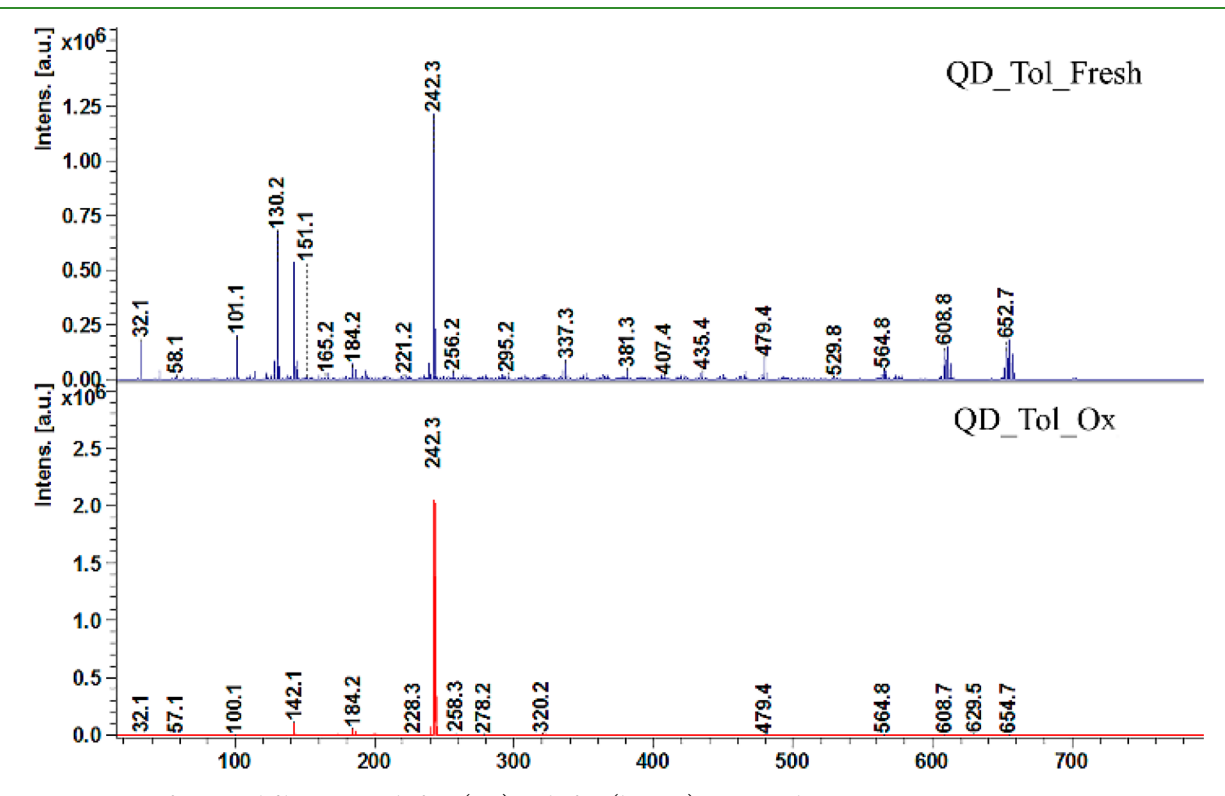


Figure 9. MS spectra of QDs-Tol film on ITO before (top) and after (bottom) ECL anodization.

arise because of the degradation of  $CH_3NH_3$  cation upon anodization with 1 and 15 CV cycles. Figure 8b shows the N 1s XPS spectra. The fresh film shows a peak at 402.4 eV

representing CH<sub>3</sub>-N species.<sup>46</sup> The peak intensity after 1 and 15 CV processing shifts to a higher binding energy region, accompanied by a peak due to the decomposition of the film.

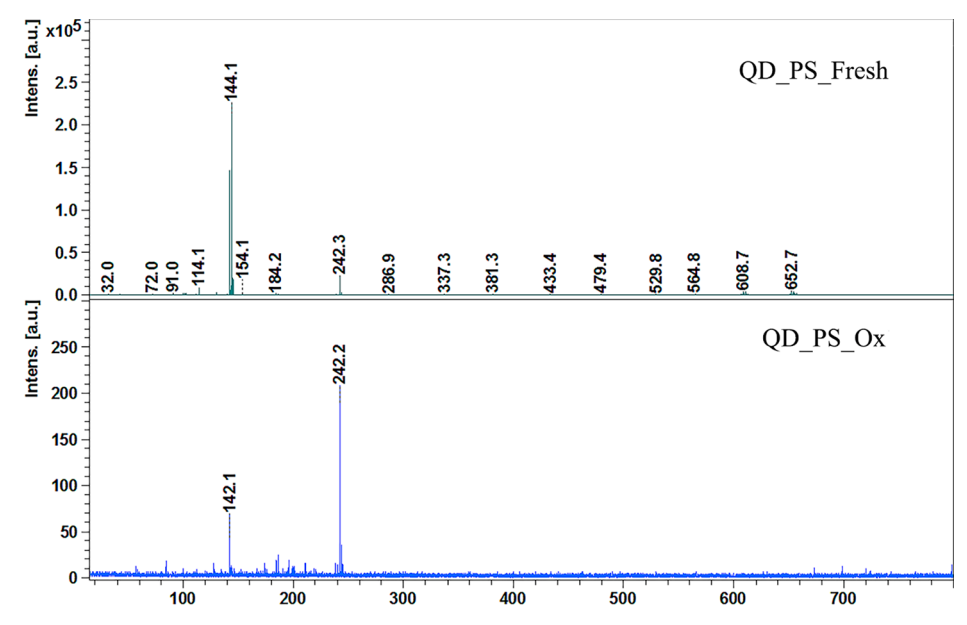


Figure 10. MS spectra of fresh QDs-PS film on ITO before (top) and after (bottom) ECL anodization.

Figure 8c shows the XPS spectra of O 1s at 531.9 eV corresponding to C=O typical for air-exposed sample known as adventitious carbon with the hydrocarbon species doubly bonded to oxygen functionality that is typically found on the surface of the sample.<sup>47</sup> Figure 8d shows the XPS spectra of Cl  $2p_{3/2}$  and Cl  $2p_{1/2}$  at 198.6 and 200.3 eV binding energies, respectively. Film processed with 1 and 15 CV cycles also shows the P 2s peak at binding energy 195 eV, which is heavily shifted to higher binding energy from 188 eV. The P 2s peak is from the electrolyte TBAPF<sub>6</sub>. Figure 8e shows the Br  $3d_{5/2}$  and 3d<sub>3/2</sub> at 69.0 and 69.9 eV. Figure 8f shows the Pb 4f XPS spectra, as can be seen in the fresh film, two characteristic peaks at 139.2 and 144.0 eV are assigned to energy levels of Pb<sup>2+</sup>, corresponding to the spin-orbit coupling of Pb  $4f_{7/2}$  and Pb 4f<sub>5/2</sub>. Along with these peaks we also observed two additional peaks with binding energies of 137.2 and 143.9 eV that are located at the lower binding energy side of Pb 4f 7/2 and Pb 4f<sub>5/2</sub>. These peaks can be assigned to metallic Pb atoms. Figure S7 shows the quantification of XPS peaks. The 93.7% decrease in Cl concentration after 1 CV cycle is more as compared to the decrease in Br concentration (86.6%). This disproportionate loss of halide ions yields perovskite intermediates with more Br than Cl, contributing to ECL spectrum's redshift for QDs-Tol sample from 492.2 to 578.7 nm (Figure 6a). The 72.1% decrease in chloride concentration after 15 CV cycles is less as compared to the decrease in the Br concentration (87.3%). XPS results show the instability of QD ECL is a result of the loss of MA (methylammonium) cations and the disproportionate loss of halide ions as a result of ECL

Mass Spectrometry of QDs-Tol and QDs-PS Films before and after ECL. Figures 9 and 10 show the MS spectra of the QDs-Tol and QDs-PS filmd casted on MALDI imaging ITO slides before and after 0.5 CV cycles. QDs-Tol and QDs-PS solutions were drop-casted onto a 75 mm long ITO slide and vacuum-dried for 12 h. In Figure 9, the QD film on ITO without oxidation is labeled as QDs-Tol-fresh, whereas the ECL anodized film is labeled as QDs-Tol-Ox. In Figure 10, the QD film in polystyrene without the oxidation is labeled as QDs-PS-Fresh, whereas the QDs film in polystyrene after ECL

anodization is labeled as QDs-PS-Ox. Generally, lead clusters (Pb<sub>n</sub>) and complexes of Pb with Cl and Br are observed (seeFigure S8 for assignment details). The peak intensities significantly decrease after oxidation for both QDs-Tol (Figure 9) and QDs-PS (Figure 10) films. In Figure 9, the peak at m/z of 32 corresponds to  $[CH_3NH_3]$ <sup>+</sup>, the peak intensity significantly decreases after the oxidation from 2926 counts for the QDs-Tol-Fresh film to only 551 counts in the QDs-Tol-Ox film. The decrease in the peak intensity of  $[CH_3NH_3]$ <sup>+</sup> cation in QDs determines the loss of MA (methylammonium) cation after ECL anodization.

Both the XPS and the MS results illustrate the loss of QDs due to the disproportionate loss of MA (methylammonium) and X ions (X = Cl, Br) responsible for the instability and ECL intensity and spectroscopy shift. The loss of crystallinity of initial QDs and quantum confinement due to the migration and loss of these ions in the electrochemical cell can be minimized by the polystyrene matrix. The PS matrix help maintain stability by preventing morphological changes of the QD films as shown in Figure S9, but the PS containing films show lower conductivity and their ECL is dominated by only the QDs exposed at the surface of the electrode accessible by the coreactant. The future work will focus on using a more conductive polymer matrix to improve ECL efficiency and stability.

## CONCLUSIONS

In summary, ECL from MAPbX<sub>3</sub> (MA = CH<sub>3</sub>NH<sub>3</sub>, X = Cl and Br) QDs can be obtained with enhanced stability and efficiency by incorporating them in a polystyrene matrix to minimize the loss of MA (methylammonium) cations and the halide ions. The ECL spectrum of the QD film without a polymer matrix shows a short-lived ECL peak at 492.0 nm and a more-stable ECL peak at 578.0 nm, whereas the QD-polystyrene film shows a single ECL peak at 590.4 nm because of QDs close to each other in a solid film. Only QDs exposed near the surface of polystyrene exhibit ECL activity when initiated by the oxidation of TPrA. XPS data suggest that disproportionate loss of halide ions from pristine QDs during electrochemical oxidation is an additional factor contributing to the redshift of

ECL spectrum. The MS analysis of both the films, QDs-Tol and QDs-PS, revealed enhanced stability of MAPbX<sub>3</sub> QDs in polymer film to support ECL stability. This study provides insights into addressing the ECL stability issue of MAPbX<sub>3</sub> (MA= CH<sub>3</sub>NH<sub>3</sub>, X = Cl and Br) perovskite. The major issues of a slow ECL response, as well as the poor conductivity of polystyrene-containing QD films, can be potentially solved by using a more-conductive polymer matrix than polystyrene in future studies.

#### METHODS

**Materials.** All purchased chemicals were of reagent grade and used as received without further purification. Methyl amine (CH<sub>3</sub>NH<sub>2</sub>, 40%, aq.), PbBr<sub>2</sub> (lead bromide, 99%), and PbCl<sub>2</sub> (lead chloride, 99%) were purchased from Alfa Aesar. Hydrobromic acid (HBr, 48% wt %, aq.) was purchased from Beantown Chemical. N,N-Dimethylformamide (DMF) was purchased from Amresco Inc. n-Octylamine (n-OCA) was obtained from EMD Millipore. Oleic acid (OA), tetrabutylammonium hexafluorophosphate (TBAPF<sub>6</sub>) and acetonitrile were purchased from Sigma-Aldrich. Toluene was purchased from Fisher Scientific. TPrA was obtained from Acros Organics. Polystyrene (average M.W 250 000) was purchased from Acros Organics

Synthesis of QDs-Tol and QDs-PS Films. MABr (methylammonium) and the QDs were synthesized according to previously reported literature using ligand-assisted reprecipitation method (LARP). 25,40 In a typical synthesis of QDs, 32 mM MABr, 19.9 mM PbCl<sub>2</sub>, and 20 mM PbBr<sub>2</sub> were dissolved in 5 mL of DMF with 20  $\mu$ L of n-octyl amine and 500  $\mu$ L of oleic acid. Two milliliters of this precursor solution was then added dropwise to 10 mL of toluene with vigorous stirring for 30 min. The obtained precipitates were washed with toluene once and dispersed in toluene for further studies. The composition of the synthesized quantum dots is described as CH3NH3PbCl1.08Br1.92 based on the initial molar ratio of halides abbreviated as QDs. A 0.09 wt % polystyrene solution was prepared in toluene. QDs-PS films were synthesized by mixing the QD solution with the prepared polystyrene solution (1:0.5 v/v) followed by 15 min of sonication. The solution was then drop casted onto ITO and vacuum-dried for 3 h. QDs-Tol films were prepared in a similar way by replacing polystyrene with the blank toluene.

XPS, Mass Spectrometry, and Other Characterizations. Matrix-assisted laser desorption ionization time of flight (MALDI-TOF) imaging mass spectrometry experiments were conducted on a Bruker Daltonics rapifleX mass spectrometer equipped with a smartbeamTM 3D laser ("Imaging 100 µm" as laser setup profile with raster width 200  $\mu$ m). MALDI images were processed with FlexImaging 5.0 and SCiLS Lab software. FlexControl 4.0 software was used to examine individual data point mass spectrum. X-ray diffraction (XRD) studies on the QDs-Tol and QDs-PS films on ITO were performed using X-ray diffractometer (Philips X'-Pert Pro X-ray, Cu-K $\alpha$  source). X-ray photoelectron spectroscopy (XPS) measurements were performed with a Kratos Axis ultra DLD. The surface morphology of the synthesized QDs-Tol film was characterized using JEOL 7000 scanning electron microscope (SEM). The UV-vis absorption spectra were studied using UV-vis spectrophotometer (PerkinElmer). All the ECS studies were performed using a threeelectrode configuration with electrochemical workstation (CHI 760C, CH Instruments Inc., Austin, TX) using ITO, Ag quasi-reference electrode (QRE), and the Pt wire as the working, reference, and counter electrodes, respectively. QRE was calibrated with a SCE electrode to confirm the stability and actual electrode potential. The ECL signal was collected by a photomultiplier tube (PMT) at 900 HV. ECL and the PL spectra were also collected by a CCD camera (Acton, SP2500 monochromator, Princeton Instruments) where the detector temperature was maintained at −100 °C with liquid nitrogen. The electrolyte used for the ECL study is 0.1 M tetrabutyl ammonium hexafluorophosphate (TBAPF<sub>6</sub>) in acetonitrile with and without 50 mM tripropyl amine (TPrA).

## ASSOCIATED CONTENT

# Supporting Information

The Supporting Information is available free of charge at https://pubs.acs.org/doi/10.1021/acsami.0c01050.

Information about the lifetime, SEM morphology, XPS quantification, MS spectrum peak assignment, normalized PL and ECL spectra, and XRD of the QDs before and after ECL anodization (PDF)

## AUTHOR INFORMATION

## **Corresponding Author**

Shanlin Pan — Department of Chemistry and Biochemistry, The University of Alabama, Tuscaloosa, Alabama 35487-0336, United States; ⊚ orcid.org/0000-0003-2226-9687; Email: span1@ua.edu

#### **Authors**

Jeetika Yadav — Department of Chemistry and Biochemistry, The University of Alabama, Tuscaloosa, Alabama 35487-0336, United States

Qiaoli Liang — Department of Chemistry and Biochemistry, The University of Alabama, Tuscaloosa, Alabama 35487-0336, United States

Complete contact information is available at: https://pubs.acs.org/10.1021/acsami.0c01050

#### **Author Contributions**

The manuscript was written through the contributions of all authors. All authors have given approval to the final version of the manuscript.

# **Funding**

We thank the National Science Foundation (NSF award CHE 1508192 and OIA 1539035) for the financial support from. We also acknowledge the support of the grant NSF CHE-1726812 from the Major Research Instrumentation Program for purchase of the MALDI/TOF-TOF mass spectrometer UA.

#### Notes

The authors declare no competing financial interest.

# ■ ACKNOWLEDGMENTS

We acknowledge the help of M. Buettner for recording the XPS of the QDs-Tol films on ITO substrate. The authors also thank P. Shinde for assisting high-resolution TEM (HRTEM) measurements and A. Steen and N. Hammer for the lifetime measurements of the perovskite QDs.

## ABBREVIATIONS

QDs, quantum dots; PS, polystyrene; ECL, electrogenerated chemiluminescence; PL, photoluminescence; QDs-Tol, quantum dots in toluene; QDs-PS, quantum dots in polystyrene; LARP, ligand-assisted reprecipitation technique; fwhm, full width at half maxima; F.I., fluorescence intensity; MA, methylammonium

## REFERENCES

(1) Bella, F.; Griffini, G.; Correa-Baena, J.-P.; Saracco, G.; Grätzel, M.; Hagfeldt, A.; Turri, S.; Gerbaldi, C. Improving Efficiency and Stability of Perovskite Solar Cells With Photocurable Fluoropolymers. *Science* **2016**, 354, 203–206.

(2) Tsai, H.; Nie, W.; Blancon, J.-C.; Stoumpos, C. C.; Asadpour, R.; Harutyunyan, B.; Neukirch, A. J.; Verduzco, R.; Crochet, J. J.; Tretiak,

- S.; et al. High-Efficiency Two-Dimensional Ruddlesden—Popper Perovskite Solar Cells. *Nature* **2016**, *536*, 312–316.
- (3) Stranks, S. D.; Snaith, H. J. Metal-Halide Perovskites for Photovoltaic and Light-Emitting Devices. *Nat. Nanotechnol.* **2015**, *10*, 391–402.
- (4) Kojima, A.; Teshima, K.; Shirai, Y.; Miyasaka, T. Organometal Halide Perovskites as Visible-Light Sensitizers for Photovoltaic Cells. *J. Am. Chem. Soc.* **2009**, *131*, 6050–6051.
- (5) Zhang, Q.; Ha, S. T.; Liu, X.; Sum, T. C.; Xiong, Q. Room-Temperature Near-Infrared High-Q Perovskite Whispering-Gallery Planar Nanolasers. *Nano Lett.* **2014**, *14*, 5995–6001.
- (6) Sutherland, B. R.; Hoogland, S.; Adachi, M. M.; Wong, C. T.; Sargent, E. H. Conformal Organohalide Perovskites Enable Lasing on Spherical Resonators. *ACS Nano* **2014**, *8*, 10947–10952.
- (7) Xing, G.; Mathews, N.; Lim, S. S.; Yantara, N.; Liu, X.; Sabba, D.; Grätzel, M.; Mhaisalkar, S.; Sum, T. C. Low-Temperature Solution-Processed Wavelength-Tunable Perovskites for Lasing. *Nat. Mater.* **2014**, *13*, 476–480.
- (8) Dohner, E. R.; Jaffe, A.; Bradshaw, L. R.; Karunadasa, H. I. Intrinsic White-Light Emission From Layered Hybrid Perovskites. *J. Am. Chem. Soc.* **2014**, *136*, 13154–13157.
- (9) Tan, Z.-K.; Moghaddam, R. S.; Lai, M. L.; Docampo, P.; Higler, R.; Deschler, F.; Price, M.; Sadhanala, A.; Pazos, L. M.; Credgington, D.; et al. Bright Light-Emitting Diodes Based on Organometal Halide Perovskite. *Nat. Nanotechnol.* **2014**, *9*, 687–692.
- (10) Kim, Y. H.; Cho, H.; Heo, J. H.; Kim, T. S.; Myoung, N.; Lee, C. L.; Im, S. H.; Lee, T. W. Multicolored Organic/Inorganic Hybrid Perovskite Light-Emitting Diodes. *Adv. Mater.* **2015**, *27*, 1248–1254.
- (11) Era, M.; Morimoto, S.; Tsutsui, T.; Saito, S. Organic-Inorganic Heterostructure Electroluminescent Device Using a Layered Perovskite Semiconductor (C<sub>6</sub>H<sub>5</sub>C<sub>2</sub>H<sub>4</sub>NH<sub>3</sub>)<sub>2</sub>PbI<sub>4</sub>. *Appl. Phys. Lett.* **1994**, 65, 676–678.
- (12) Ahmed, T.; Seth, S.; Samanta, A. Boosting the Photoluminescence of  $CsPbX_3$  (X=Cl, Br, I) Perovskite Nanocrystals Covering a Wide Wavelength Range by Postsynthetic Treatment With Tetrafluoroborate Salts. *Chem. Mater.* **2018**, *30*, 3633–3637.
- (13) Bai, S.; Yuan, Z.; Gao, F. Colloidal Metal Halide Perovskite Nanocrystals: Synthesis, Characterization, and Applications. *J. Mater. Chem. C* **2016**, *4*, 3898–3904.
- (14) Cai, Z.; Li, F.; Xu, W.; Xia, S.; Zeng, J.; He, S.; Chen, X. Colloidal CsPbBr<sub>3</sub> Perovskite Nanocrystal Films as Electrochemiluminescence Emitters in Aqueous Solutions. *Nano Res.* **2018**, *11*, 1447–1455.
- (15) Chirvony, V. S.; Gonzalez-Carrero, S.; Suarez, I.; Galian, R. E.; Sessolo, M.; Bolink, H. J.; Martinez-Pastor, J. P.; Perez-Prieto, J. Delayed Luminescence in Lead Halide Perovskite Nanocrystals. *J. Phys. Chem. C* **2017**, *121*, 13381–13390.
- (16) Fan, Y.; Xing, H.; Zhai, Q.; Fan, D.; Li, J.; Wang, E. Chemiluminescence of CsPbBr<sub>3</sub> Perovskite Nanocrystal on the Hexane/Water Interface. *Anal. Chem. (Washington, DC, U. S.)* **2018**, 90, 11651–11657.
- (17) Freppon, D. J.; Men, L.; Burkhow, S. J.; Petrich, J. W.; Vela, J.; Smith, E. A. Photophysical Properties of Wavelength-Tunable Methylammonium Lead Halide Perovskite Nanocrystals. *J. Mater. Chem. C* 2017, 5, 118–126.
- (18) Galisteo-Lopez, J. F.; Calvo, M. E.; Rojas, T. C.; Miguez, H. Mechanism of Photoluminescence Intermittency in Organic-Inorganic Perovskite Nanocrystals. *ACS Appl. Mater. Interfaces* **2019**, *11*, 6344–6349.
- (19) Gibson, N. A.; Koscher, B. A.; Alivisatos, A. P.; Leone, S. R. Excitation Intensity Dependence of Photoluminescence Blinking in CsPbBr<sub>3</sub> Perovskite Nanocrystals. *J. Phys. Chem. C* **2018**, *122*, 12106–12113.
- (20) Halder, A.; Pathoor, N.; Chowdhury, A.; Sarkar, S. K. Photoluminescence Flickering of Micron-Sized Crystals of Methylammonium Lead Bromide: Effect of Ambience and Light Exposure. *J. Phys. Chem. C* **2018**, *122*, 15133–15139.
- (21) Huang, H.; Polavarapu, L.; Sichert, J. A.; Susha, A. S.; Urban, A. S.; Rogach, A. L. Colloidal Lead Halide Perovskite Nanocrystals:

- Synthesis, Optical Properties and Applications. NPG Asia Mater. 2016. 8, e328.
- (22) Zhang, Y.; Liu, J.; Wang, Z.; Xue, Y.; Ou, Q.; Polavarapu, L.; Zheng, J.; Qi, X.; Bao, Q. Synthesis, Properties, and Optical Applications of Low-Dimensional Perovskites. *Chem. Commun.* (Cambridge, U. K.) 2016, 52, 13637–13655.
- (23) Tan, X.; Zhang, B.; Zou, G. Electrochemistry and Electrochemiluminescence of Organometal Halide Perovskite Nanocrystals in Aqueous Medium. *J. Am. Chem. Soc.* **2017**, *139*, 8772–8776.
- (24) Huang, Y.; Long, X.; Shen, D.; Zou, G.; Zhang, B.; Wang, H. Hydrogen Peroxide Involved Anodic Charge Transfer and Electrochemiluminescence of All-Inorganic Halide Perovskite CsPbBr<sub>3</sub> Nanocrystals in an Aqueous Medium. *Inorg. Chem.* **2017**, *56*, 10135–10138.
- (25) Zhang, F.; Zhong, H.; Chen, C.; Wu, X.-g.; Hu, X.; Huang, H.; Han, J.; Zou, B.; Dong, Y. Brightly Luminescent and Color-Tunable Colloidal CH<sub>3</sub>NH<sub>3</sub>PbX<sub>3</sub> (X = Br, I, Cl) Quantum Dots: Potential Alternatives for Display Technology. *ACS Nano* **2015**, *9*, 4533–4542.
- (26) Huang, Y.; Fang, M.; Zou, G.; Zhang, B.; Wang, H. Monochromatic and Electrochemically Switchable Electrochemiluminescence of Perovskite CsPbBr<sub>3</sub> Nanocrystals. *Nanoscale* **2016**, 8, 18734–18739.
- (27) Huang, H.; Susha, A. S.; Kershaw, S. V.; Hung, T. F.; Rogach, A. L. Control of Emission Color of High Quantum Yield CH<sub>3</sub>NH<sub>3</sub>PbBr<sub>3</sub> Perovskite Quantum Dots by Precipitation Temperature. *Adv. Sci.* (Weinh) **2015**, *2*, 1500194.
- (28) Li, L.; Zhang, Z.; Chen, Y.; Xu, Q.; Zhang, J. R.; Chen, Z.; Chen, Y.; Zhu, J. J. Sustainable and Self-Enhanced Electrochemiluminescent Ternary Suprastructures Derived from CsPbBr<sub>3</sub> Perovskite Quantum Dots. *Adv. Funct. Mater.* **2019**, 29, 1902533.
- (29) Fan, Y.; Xing, H.; Zhai, Q.; Fan, D.; Li, J.; Wang, E. Chemiluminescence of CsPbBr<sub>3</sub> Perovskite Nanocrystal on the Hexane/Water Interface. *Anal. Chem.* **2018**, *90*, 11651–11657.
- (30) Miao, W. Electrogenerated Chemiluminescence and Its Biorelated Applications. *Chem. Rev.* **2008**, *108*, 2506–2553.
- (31) Xue, J.; Zhang, Z.; Zheng, F.; Xu, Q.; Xu, J.; Zou, G.; Li, L.; Zhu, J. J. Efficient Solid-State Electrochemiluminescence From High-Quality Perovskite Quantum Dot Films. *Anal. Chem.* **2017**, *89*, 8212–8216.
- (32) Cai, Z.; Li, F.; Xu, W.; Xia, S.; Zeng, J.; He, S.; Chen, X. Colloidal CsPbBr<sub>3</sub> Perovskite Nanocrystal Films as Electrochemiluminescence Emitters in Aqueous Solutions. *Nano Res.* **2018**, *11*, 1447–1455.
- (33) Lu, H.; Chen, X.; Anthony, J. E.; Johnson, J. C.; Beard, M. C. Sensitizing Singlet Fission With Perovskite Nanocrystals. *J. Am. Chem. Soc.* **2019**, *141*, 4919–4927.
- (34) Qiu, L.; Lin, L.; Huang, Y.; Lai, Z.; Li, F.; Wang, S.; Lin, F.; Li, J.; Wang, Y.; Chen, X. Unveiling the Interfacial Electrochemiluminescence Behavior of Lead Halide Perovskite Nanocrystals. *Nanoscale Adv.* **2019**, *1*, 3957–3962.
- (35) Cao, Y.; Zhang, Z.; Li, L.; Zhang, J. R.; Zhu, J. J. An Improved Strategy for High-Quality Cesium Bismuth Bromine Perovskite Quantum Dots With Remarkable Electrochemiluminescence Activities. *Anal. Chem.* **2019**, *91*, 8607–8614.
- (36) Boyd, C. C.; Cheacharoen, R.; Leijtens, T.; McGehee, M. D. Understanding Degradation Mechanisms and Improving Stability of Perovskite Photovoltaics. *Chem. Rev.* **2019**, *119*, 3418–3451.
- (37) Jena, A. K.; Kulkarni, A.; Miyasaka, T. Halide Perovskite Photovoltaics: Background, Status, and Future Prospects. *Chem. Rev.* **2019**, *119*, 3036–3103.
- (38) Lee, S.; Kim, D. B.; Yu, J. C.; Jang, C. H.; Park, J. H.; Lee, B. R.; Song, M. H. Versatile Defect Passivation Methods for Metal Halide Perovskite Materials and Their Application to Light-Emitting Devices. *Adv. Mater.* (Weinheim, Ger.) 2019, 31, 1805244.
- (39) Petrovic, M.; Chellappan, V.; Ramakrishna, S. Perovskites: Solar Cells & Engineering Applications Materials and Device Developments. *Sol. Energy* **2015**, *122*, *678*–*699*.

- (40) Wusimanjiang, Y.; Yadav, J.; Arau, V.; Steen, A. E.; Hammer, N. I.; Pan, S. Blue Electrogenerated Chemiluminescence from Halide Perovskite Nanocrystals. *J. Anal.Test.* **2019**, *3*, 125–133.
- (41) Guo, W.; Chen, N.; Xu, B.; Lu, Y.; Li, B.; Wu, T.; Cheng, Q.; Li, Y.; Chen, J.; Lin, Y.; Chen, Z. Stability of Hybrid Organic-Inorganic Perovskite CH<sub>3</sub>NH<sub>3</sub>PbBr<sub>3</sub> Nanocrystals Under Co-Stresses of UV Light Illumination and Temperature. *Nanomaterials* **2019**, *9*, 1158–1169.
- (42) Ding, Z.; Quinn, B. M.; Haram, S. K.; Pell, L. E.; Korgel, B. A.; Bard, A. J. Electrochemistry and Electrogenerated Chemiluminescence From Silicon Nanocrystal Quantum Dots. *Science* **2002**, *296*, 1293–1297.
- (43) Sun, L.; Bao, L.; Hyun, B.-R.; Bartnik, A. C.; Zhong, Y.-W.; Reed, J. C.; Pang, D.-W.; Abruña, H. D.; Malliaras, G. G.; Wise, F. W. Electrogenerated Chemiluminescence From PbS Quantum Dots. *Nano Lett.* **2009**, *9*, 789–793.
- (44) Xu, R.-P.; Li, Y.-Q.; Jin, T.-Y.; Liu, Y.-Q.; Bao, Q.-Y.; O'Carroll, C.; Tang, J.-X. In Situ Observation of Light Illumination-Induced Degradation in Organometal Mixed-Halide Perovskite Films. *ACS Appl. Mater. Interfaces* **2018**, *10*, 6737–6746.
- (45) Yuan, S.; Gu, J.; Zheng, Y.; Jiang, W.; Liang, B.; Pehkonen, S. O. Purification of Phenol-Contaminated Water by Adsorption With Quaternized Poly(dimethylaminopropyl methacrylamide)-Grafted PVBC Microspheres. *J. Mater. Chem. A* **2015**, *3*, 4620–4636.
- (46) Xiong, W.; Dai, W.; Hu, X.; Yang, L.; Wang, T.; Qin, Y.; Luo, X.; Zou, J. Enhanced Photocatalytic Reduction of CO<sub>2</sub> into Alcohols on Z-Scheme Ag/Ag<sub>3</sub>PO<sub>4</sub>/CeO<sub>2</sub> driven by visible light. *Mater. Lett.* **2018**, 232, 36–39.
- (47) Rocks, C.; Svrcek, V.; Maguire, P.; Mariotti, D. Understanding Surface Chemistry During MAPbI<sub>3</sub> Spray Deposition and its Effect on Photovoltaic Performance. *J. Mater. Chem. C* **2017**, *5*, 902–916.